Synthesis and properties of La0.05Ba0.95Ti1-xMyO3 (M = Mn, Ce) as anode materials for solid oxide fuel cells

Cédric Périllat-Merceroz, Edouard Capoen, Pascal Roussel, Sébastien Rosini, Patrick Gélin, Rose-Noëlle Vannier, Gilles Gauthier

Synthesis and properties of $La_{0.05}Ba_{0.95}Ti_{1-x}M_yO_3$ (M = Mn, Ce) as anode materials for solid oxide fuel cells

Cédric Périllat-Merceroz [a,b], Pascal Roussel [b], Edouard Capoen [a], Sébastien Rosini [a], Patrick Gélin [c], Rose-Noëlle Vannier [b], Gilles Gauthier [a,d,*]

[a] CEA, LITEN, Grenoble 38054, France
[b] Université de Lille, CNRS UMR 8181, Unité de Catalyse et de Chimie du Solide (UCCS), ENSCL, Lille F-59000, France
[c] Université Lyon 1, CNRS, UMR 5256, IRCELYON, Institut de Recherches sur la Catalyse et l'Environnement de Lyon, 2 avenue Albert Einstein, Villeurbanne 69626, France
[d] Universidad Industrial de Santander, Grupo INTERFASE, Ciudad universitaria, Calle 9, Carrera 27, Bucaramanga (Santander), Colombia

Stoichiometric and sub-stoichiometric lanthanum barium titanates (LBT) of perovskite structure type, substitut-ed or not with Mn and/or Ce at the Ti-site, were prepared by sol–gel route with heat treatment in air. All the com-pounds display a cubic *Pm-3m* symmetry, which remains stable in reducing atmosphere. Whereas Mn substitution highly promotes the reducibility of the material, the electrical and electrochemical performance of Mn-doped compounds is decreased with respect to non-doped sub-stoichiometric LBT. In contrast, the electrical conductivity and resistance polarization of Ce-substituted LBT are close to those of non-doped LBT and Ce-substituted LBT appears especially efficient in improving the catalytic properties for methane steam reforming and avoiding carbon formation.

1. Introduction

The solid oxide fuel cell (SOFC) is an interesting energy production alternative for human future. A high thermodynamic efficiency and a very low environmental impact, associated to the possible use of alternative fuels to hydrogen (including organic wastes), make this electrochemical system very attractive, especially considering the slow evolution to the so-called hydrogen-based economy. Nevertheless, one of the main issues that have to be addressed considering SOFCs is the reduction of degradation and irreversible losses of activity of Ni-based materials when organic fuels like natural gas are directly used at the anode: carbon deposition, sulfur poisoning as well as coarsening of Ni particles, and redox cycling are the principal problems, the two latter being true even in H_2/H_2O atmospheres [1–3].

Due to their high resistance toward reducing and sulfured atmospheres [4], perovskite-type compounds (of general formula ABO_3) have found a lot of interest in the SOFC research community. Various $SrTiO_3$-based titanates have already been considered, in which Sr^{2+} has been generally substituted by a trivalent cation such as La^{3+} or Y^{3+} in order to increase the too low electrical conductivity displayed by $Sr^{2+}Ti^{4+}O_3$ [5–15]. Indeed, in reducing conditions, the presence of trivalent ions at the A-site of the perovskite makes the reduction of titanium easier, from Ti^{4+} to Ti^{3+}, enhancing electronic charge carrier concentration [16–18]. It is worth noting that the reduced state of the material seems to play an important role on the anode performance when considering a global cell: the polarization resistance, R_p, can decrease from 52 to 2.97 Ω cm^2 at 900 °C in wet H_2 for the same composition reduced at different temperatures [5,19]. Although relatively high current density of 119 mA cm^{-2} and power density of 76 mW cm^{-2} were obtained for such non-cermet materials, the four-time increase of R_p in wet CH_4 highlighted the definitely poor (electro)-catalytic activity of the non-doped material [5]. Thus, to improve the catalytic and electrochemical power of lanthanum strontium titanates, several studies focused on the impregnation of ceramic networks, and small quantities of very active nanoparticles, e.g., Ni, CeO_2 or Ru, can be added to the electrode. Such material is generally obtained by impregnation of a pre-sintered conducting electrode with a metallic salt or a nanopowder suspension [20–25].

Another classical strategy, also described in literature, deals with the introduction in the titanate structure of active elements such as Mn, Ga, V, Cr, Fe, Nb, Co, and Ni [26–40]. Although already attempted, Ce substitution at the Ti-site of strontium titanates has never been achieved. Only partial substitution of the La-site could be obtained [19,41,42] stemming

* Corresponding author at: Université Lyon 1, CNRS, UMR 5256, IRCELYON, Institut de Recherches sur la Catalyse et l'Environnement de Lyon, 2 avenue Albert Einstein, Villeurbanne 69626, France. Tel.: +57 734 4000x2528.
E-mail address: gilgau@uis.edu.co (G. Gauthier).

from the really different effective ionic radius between Ce^{4+} vs. Ti^{4+} ($r_{Z=6}(Ce^{4+}) = 0.87$ Å vs. $r_{Z=6}(Ti^{4+}) = 0.605$ Å [43]).

Considering the high activity of ceria in several catalytic mechanisms such as methane steam reforming [44], but the low electronic conductivity of the fluorite, the purpose of our study was to explore the possibility of inserting Ce in place of Ti in perovskite titanates. The interest for the La-doped barium titanates (LBT) stems also from recently reported results described for Ba doping in LST [45] or for pure $BaTiO_3$ itself as an SOFC anode operating in H_2S-containing methane [46]. In addition to the effect of $Ce^{4+/3+}$ as active catalytic and electrochemical redox couple, we also embarked in a comparative study with another possible dopant of the (La,Ba)TiO_3 family, namely, manganese, owing to the increased electrochemical behavior related to such doping element in LSTs [27,28,38,47]. Hence, after a detailed description of the synthesis and structural characterization of the materials, the present work deals with the effect of M = Mn, Ce when substituted to Ti on the catalytic and anodic properties of stoichiometric $La_{0.05}Ba_{0.95}Ti_{1-x}M_xO_3$ and sub-stoichiometric $La_{0.05}Ba_{0.95}Ti_{1-x/4-y}M_yO_3$.

2. Experimental procedure

The standard Pechini route was used to prepare the $x = y = 0.05$ members of the B-site sub-stoichiometric $La_{0.05}Ba_{0.95}Ti_{1-x/4-y}M_yO_3$ series with M = Mn, Ce, i.e., $La_{0.05}Ba_{0.95}Ti_{0.9875}O_3$ (LBTss), $La_{0.05}Ba_{0.95}Ti_{0.9375}Ce_{0.05}O_3$ (LBTCss), and $La_{0.05}Ba_{0.95}Ti_{0.9375}Mn_{0.05}O_3$ (LBTMss) [48]. Details concerning the protocol for the gel preparation can be found in the study of Périllat-Merceroz et al. [42,49]. The solutions were evaporated on a magnetic stirring plate until obtaining gels that were then dried and pyrolyzed in an oven overnight at 250 °C. After grinding, the resulting powders were heat treated in air at 700 °C for 5 h in order to remove the excess of nitrates and organic residues. After grinding, the powders were pressed into pellets before being heat treated at 1400 °C for 24 h in air. Then the obtained compounds were exposed to an Ar/H_2(2%) atmosphere at 900 °C for 48 h to probe their chemical stability in SOFC anodic conditions.

Powder X-ray diffraction (XRD) data were collected at room temperature (RT) using a Bruker AXS D8 Advance diffractometer working in Bragg–Brentano geometry and equipped with a secondary graphite monochromator and a scintillation detector. Cu K-$\alpha_{1,2}$ radiations were used in the range $2\theta = 15$–120°, with a 0.02° step and a 10 s counting time per step, respectively. The Fullprof Suite program was used for pattern-matching refinement, using the Thompson–Cox–Hastings pseudo-Voigt profile function [50].

For catalytic tests, the powders were ground in a tungsten carbide vibrating mill and sifted between 40 and 50 μm in order to control gas diffusion. The grinding step was performed until a specific surface area value around 10 $m^2\ g^{-1}$ has been reached; the BET area measurements were obtained by nitrogen adsorption using a Beckman Coulter SA3100 analyzer. Catalytic activity experiments were carried out in a continuous flow system at atmospheric pressure using a tubular U-shaped quartz micro-reactor. Blank experiments (without any sample) were performed to check that the reactor was non-reactive. Samples (about 20 mg) were deposited on a quartz plug introduced into the reactor and renewed for each test. Water content was determined using an Edgetech Dew Prime I dew point monitor placed nearby the reactor outlet. An ECP®-type (M&C) gas cooler was used to trap most of the water vapor, thus allowing gas analysis by a Varian micro-GC equipped with appropriate columns (molecular sieve 5A and Porapak) and a thermal conductivity detector. Details concerning the catalytic test procedure can be found elsewhere [49].

DC electrical conductivity measurements were carried out in N_2/H_2(97/3) reducing atmosphere as a function of temperature, using the four probe technique (Tacussel Electronique PGS201T as programmable current source and Hewlett Packard 34401A digital multimeter for the voltage determination). For those electrical characterizations, each powder was compacted under 0.2 MPa and isostatically pressed under 300 MPa. The obtained pellets were sintered at 1600 °C for 15 h in air, achieving a final relative density of LBTM = 90%, LBTMss = 95%, and LBTCss = 96% of the respective theoretical density. Then the pellets were cylinder-shaped using diamond tools until achieving a final diameter of 6 mm. Subsequently, two grooves were shaped, separated by a distance of 6 mm. Potential measurement electrodes were obtained by gold wires inserted into the grooves and slightly covered by a gold ink layer (Metalor®); the same gold ink was painted on both faces of the cylinder to allow the determination of the current flow through the pellets. The samples were annealed at 650 °C for 1 h in air prior to measurements to remove all the organics from the paste. Data were normalized taking into account the geometric factor and corrected from the total porosity (π_{total}) of the specimens using the empirical formula $\sigma_{corrected} = \sigma_{measured} / (1 - (\pi_{total} / 100))^2$ [51]. The Arrhenius law $\sigma = (A/T)\exp(-E_a/kT)$ was used for graphical representation and treatment of electrical conductivity vs. temperature data, in which A is a constant term, T is temperature, k is the Boltzmann constant, and E_a is the activation energy.

Thermo-gravimetric analyses (TGA) were performed in air using a SETARAM TG 92–16.18 device equipped with a 1300-μL Pt crucible (about 1 g of sample). Heating and cooling rates were 2 °C min^{-1} and 4 °C min^{-1}, respectively, with an isotherm plateau for 2 h at 1000 °C.

Electrochemical measurements were carried out using a ProboStat™ device from NorECs. Partial oxygen pressure pO_2 was controlled by a SETNAG oxygen pump. Complex impedance measurements were registered at OCV in H_2/H_2O(97/3) (10 L h^{-1}) with a Solartron 1260 frequency response analyzer controlled by Zplot software ($\Delta f = 10^6$–10^{-2} Hz, $\Delta V = \pm 30$ mV) and plotted in the Nyquist representation. Polarization resistance R_p was normalized by the active surface area of the electrode ($\Omega\ cm^2$) and divided by two according to the measurement configuration. Symmetrical cells (same electrode on both sides) were screen-printed on homemade 8YSZ (8 mol% yttria-stabilized zirconia) disks as electrolyte (125 μm thick). As for catalytic tests, the powders were ground prior to ink preparation in order to decrease the grain size and achieve a specific surface area of about 10 $m^2\ g^{-1}$. Each ink was made from a mixture of the powder and a binder (terpineol:ethyl cellulose = 95:5 wt.%) with a 1:1 weight ratio. Current collection was supplied by a nickel metal layer: after sintering, NiO-ink was screen-printed, sintered at 700 °C for 1 h and then at 1000 °C for 1 h in air, acting as a current collector. Then the global cells were exposed to Ar/H_2(98/2) at 900 °C for 48 h to reduce NiO into conducting Ni metal.

The cross-sectional microstructure of the fractured symmetrical cells was examined after electrochemical measurements using a field emission gun scanning electron microscope (FEG-SEM, ZEISS Leo 1530 Gemini).

3. Results

3.1. Structural characterization of the oxidized materials

In the Ba-Ti-O system, the accommodation of any charge excess stemming from aliovalent substitution of Ba^{2+} by trivalent donor La^{3+} is compensated by two possible mechanisms: electronic or ionic compensation. In reducing synthesis atmosphere, the Ti^{4+} to Ti^{3+} partial reduction was proposed leading to the formation of $La_xBa_{1-x}Ti_x^{3+}Ti_{1-x}^{4+}O_3$ [52,53]. In oxidizing atmosphere, cationic compensation leads to the formation of Ti^{4+} vacancies. Sub-stoichiometric solid solution $La_xBa_{1-x}Ti_{1-x/4}^{4+}O_3$ co-exists with one or more Ti-rich phases depending on the barium content [54–56]. It is worth noting that some studies mention the existence of Ba^{2+} vacancies with the formation of an $La_{2/3x}Ba_{1-x}TiO_3$ solid solution for $x < 0.003$ [57–61]. Similar observations were stated when Ba^{2+} was substituted by other trivalent donors as Ce^{3+} [62–64] or Nd^{3+} [54,55,65]. Ce substitution at Ti-site was investigated in the stoichiometric $BaTi_{1-y}Ce_yO_3$, as well as in the

sub-stoichiometric $La_xBa_{1-x}Ti_{1-x/4-y}Ce_yO_3$ with dielectric and ferroelectric properties [66,67]. In contrast to Ce substitution, in oxidizing atmosphere, the insertion at the Ti-site of a transition metal, e.g., Mn, allows the accommodation of La^{3+} in a stoichiometric perovskite, without the creation of cationic vacancies [68,69].

The XRPD patterns of all prepared compounds, after synthesis at 1400 °C in air, are displayed in Fig. 1. The absence of any impurity peaks proves the existence of single phased perovskite for such compositions, all being indexed in the cubic symmetry. It confirms that, in air, the classical form to insert active elements at the Ti-site of lanthanum barium titanate, and particularly Ce, is the adoption of a B-site sub-stoichiometric perovskite. Indeed, the formation of cation vacancies represents the easiest way for those materials to accommodate the excess of electronic charge carried by the 5 mol% of La^{3+} at the Ba^{2+} site, as in the literature´s example $Ba_{0.97}La_{0.03}Ti_{0.9425}Ce_{0.05}O_3$ [67]. However, the substitution of Mn for Ti makes possible the La for Ba doping without any need for cation sub-stoichiometry; this is due to the oxidation state flexibility of manganese that can easily vary from +2 to +4 in perovskites and compensate the donor doping. The formation of cation vacancies in LBTss would be then replaced by electronic compensation mechanism via Mn reduction from probably Mn^{4+} to Mn^{3+}, as described by Parkash et al. [68] in the $La_xBa_{1-x}Ti_{1-x}Mn_xO_3$ series with $x \leq 0.1$ or more recently by Benamira et al. [69]. As attested by the case of LBTCM, Mn co-doping seems to be an interesting way to stabilize pure and stoichiometric Ce-substituted LBT.

Although no impurity peaks were detected by XRD, the presence of undetectable nano-scaled inhomogeneity could also be retained by the perovskite structure. Cation distribution in the whole structure strongly depends on synthesis conditions (preparation mode, sintering temperature, and duration). Some studies highlight the presence of inhomogeneity defects remaining after low sintering conditions (1300 °C for some hours) in La-substituted barium titanates [70,71]. The same conclusion was proposed concerning $BaTiO_3$-$BaCeO_3$ solid solution when sintering temperature remains below 1400 °C [67]. However, in such cases, internal strains induced by substitution were produced by the proper homogenization difficulties related to the traditional solid-state synthesis. Here, employing sufficient heat treatment combined to sol–gel route can be considered as efficient to achieve randomly dispersed cation distribution through the whole lattice of the as-synthesized materials. Furthermore, EPR measurements performed on LBTCss compound already confirmed a structure conform to the initial stoichiometry, excluding the hypothetic presence of Ce^{3+} at the Ba^{2+}/La^{3+} site [67].

Interestingly, whereas non-doped $BaTiO_3$ adopts a tetragonal *P4mm* symmetry at room temperature, here all the prepared compounds present the highest cubic symmetry characteristic of ideal perovskite. A similar behavior concerning the perovskite symmetry has been recently observed in the case of $Ba_{0.5}La_{0.5}Ti_{0.3}M_{0.7}O_3$ [69]. Pattern-matching refinements were therefore performed using XRD data in the *Pm-3m* space group. The refined unit-cell parameters are given in Table 1. All the refinements present good agreements factors with *R*, R_p, and *G.o.f.* (χ^2) values between 8.72% and 14.4%, 13.3% and 26.2%, and finally 1.35% and 4.18, respectively. The substitution of Mn for Ti in LBTss leads to a cell dimension decrease for LBTMss, whereas Ce for Ti substitution corresponds to a cell parameter increase for LBTCss. The same situation can be observed when comparing LBTM and LBTCM. Such influence of the La^{3+} for Ba^{2+} substitution on the cell parameter is conform to the literature, as confirmed by the available data for LBTss ($a_{LBTss} = 4.00200(8)$ Å (this study) vs. $a = 4.0022(4)$ Å by Morrison et al. [72,73]). Further, Mn/Ce for Ti substitution logically modifies the cell parameter too, in agreement with their respective ionic radius [43].

Table 1
Results of pattern-matching refinement performed in the *Pm-3m* symmetry using the XRPD data of $La_{0.05}Ba_{0.95}Ti_{0.9875}O_3$ (LBTss), $La_{0.05}Ba_{0.95}Ti_{0.9375}Mn_{0.05}O_3$ (LBTMss), $La_{0.05}Ba_{0.95}Ti_{0.9375}Ce_{0.05}O_3$ (LBTCss), $La_{0.05}Ba_{0.95}Ti_{0.95}Mn_{0.05}O_3$ (LBTM), and $La_{0.05}Ba_{0.95}Ti_{0.9}Ce_{0.05}Mn_{0.05}O_3$ (LBTCM) (i) after synthesis at 1400 °C for 24 h in air and (ii) after reduction at 900 °C for 48 h in $Ar/H_2(98/2)$.

	1400 °C-air	900 °C-$Ar/H_2(98/2)$
LBTss	a = 4.00200(8) Å	a = 4.00061(3) Å
LBTMss	a = 4.00064(7) Å	a = 4.00707(4) Å
LBTCss	a = 4.02611(7) Å	a = 4.02495(6) Å
LBTM	a = 3.99985(7) Å	a = 4.00947(8) Å
LBTCM	a = 4.02150(5) Å	a = 4.02544(7) Å

3.2. Behavior in reducing atmosphere

When exposed to a reducing $Ar/H_2(98/2)$ atmosphere at 900 °C for 48 h, all the materials remain single phased and cubic, as attested by their respective XRD patterns (Fig. 2). In contrast to $BaTiO_3$, which exhibits a tetragonal structure evolving to cubic from ambient to high temperature [74], substituted lanthanum barium titanates remain cubic whatever the atmosphere, attesting for the good stability of the materials vs. reduction. This is an important point for an SOFC electrode material, as structural phase transition must be preferably avoided for the application, especially considering the redox and thermal cycles that must tolerate the anode material. The refined unit-cell parameters of samples after reduction are also displayed in Table 1. Whereas reducing conditions lead to a cell volume decrease in the case of LBTss and LBTCss, a cell expansion occurs for LBTMss, LBTM, and LBTCM.

TGA oxidation in air was performed on the as-reduced materials (Fig. 3). The re-oxidation corresponds to the following equation, using the Kröger–Vink notation as follows:

$$B_{Ti}^{X} + \frac{1}{2}O_O^X \rightarrow B_{Ti}^{'} + \frac{1}{2}V_O^{\bullet\bullet} \quad (1)$$

with B = Ti, Mn, and Ce. For LBTss, LBTCss, LBTMss, LBTM, and LBTCM, the weight gain was 0.059%, 0.044%, 0.093%, 0.150%, and 0.177%, respectively. LBTMss and LBTM re-oxidize between 150 °C and 450 °C,

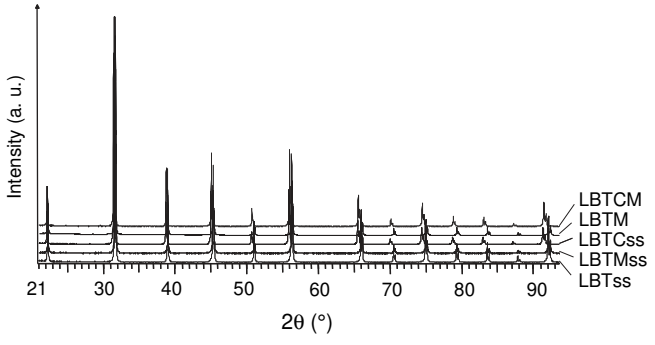

Fig. 1. Powder XRD patterns of LBTss, LBTMss, LBTCss, LBTM, and LBTCM after synthesis in air.

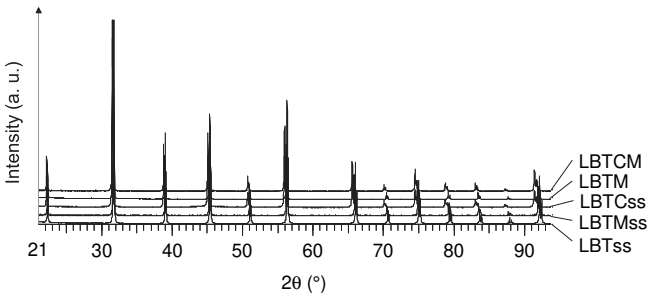

Fig. 2. XRD patterns of LBTss, LBTMss, LBTCss, LBTM, and LBTCM after synthesis in air and reduction at 900 °C for 48 h in $Ar/H_2(98/2)$.

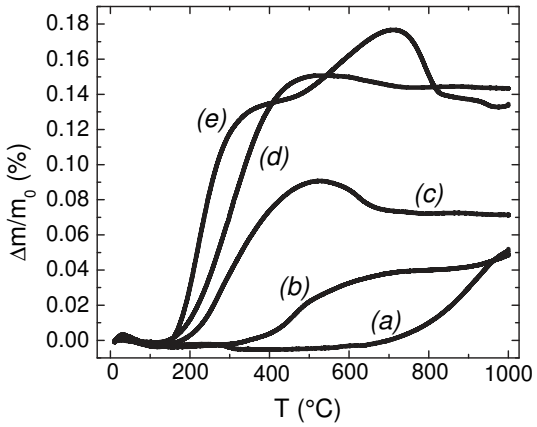

Fig. 3. TGA curves in air for (a) LBTss, (b) LBTCss, (c) LBTMss, (d) LBTM, and (e) LBTCM after synthesis and reduction at 900 °C for 48 h in Ar/H_2(98/2).

whereas LBTss re-oxidation occurs above 750 °C. LBTCM's oxidation present two steps: a first weight gain of 0.14% between 150 °C and 350 °C, and a second weight gain between 550 °C and 750 °C. It is also worth noting a weight loss of 0.02%, 0.01%, and 0.03% between 550 °C and 850 °C for LBTMss, LBTM, and LBTCM, respectively.

In LBTss, TGA quantification led to a concentration $[Ti^{3+}]_{LBTss} = 1.7\%$ of the Ti-site, the only cation possibly influenced by the reduction process. Thus, the lattice contraction observed for the reduced titanate can be indubitably attributed to the change of oxidation state from Ti^{4+} into Ti^{3+}, in association to a decrease of the oxygen content in the structure. Such situation cannot be understood by a classical cation radius increase due to Ti^{4+} to Ti^{3+} reduction [43] and is tentatively related to the disappearance of interstitial oxygen defects, in a similar way to what was observed for La-doped $SrTiO_3$ perovskites [18].

Although LBTCss cell volume suffers also a contraction, the LBTCss re-oxidation temperature is markedly different from LBTss (350 °C vs. 750 °C, respectively), as depicted in Fig. 3, and the evolution is more likely due to the reduction of Ce^{4+} into Ce^{3+} leading to a concentration $[Ce^{3+}]_{LBTss} = 1.3\%$, without excluding that part of Ti^{4+} may have been reduced too.

In contrast to what was observed for the latter two compounds, the cell of Mn-containing phases suffers expansion when those materials were reduced (Table 1). Based on literature, the weight gain attested by TGA analysis from 150 °C would be related to the reduced Mn species concentration $[Mn^{4+} \rightarrow Mn^{3+}]_{LBTMss} = 2.7\%$ and $[Mn^{4+} \rightarrow Mn^{3+}]_{LBTM} = 4.4\%$ [69]. With a higher amount of reduced species, Mn reduction seems to be easier than Ti and Ce. The presence of two steps in the oxidation process of LBTCM highlights the effect of both Mn and Ce elements (Fig. 3): Mn would be responsible of the first weight gain between 150 °C and 450 °C, similarly to what occurred for LBTMss and LBTM, whereas Ce would be responsible for the second weight gain between 400 °C and 750 °C, similarly to LBTCss. Both weight gain would be relative to $[Mn^{4+} \rightarrow Mn^{3+}]_{LBTCM} = 4.2\%$ and $[Ce^{3+}]_{LBTCM} = 1.1\%$.

Regarding the weight loss observed between 550 °C and 850 °C for the Mn-containing compounds LBTMss, LBTM, and LBTCM, we can tentatively attribute them to the formation of proton defects during the material reduction, as recently proposed by Benamira et al. [69] for La and Mn-doped barium indo-titanate. If such hypothesis is probable for LBTMss and LBTM, the higher temperature at which the weight drop is observed in the case of LBTCM ($T > 700$ °C) could be better associated to reduction of manganese in air, part of Mn^{4+} being thermally reduced into Mn^{3+}. By consequence, it could also be an explanation to the LBTMss and LBTM TG behavior between 550 °C and 700 °C. This is indeed beyond the scope of the present study to make emphasis on such feature of the materials series but could be the object of further research.

3.3. Catalytic activity for methane steam reforming

The catalytic activity with respect to the methane steam reforming reaction was evaluated for LBTss, LBTCss, LBTMss, and LBTCM at 900 °C, using a $CH_4:H_2O:N_2 = 10:1:9$ mixture whose conditions are thermodynamically favoring the coking reaction and leads theoretically (in particular in the case of Ni-based cermets) to an extensive accumulation of carbon. The only reaction products were H_2, CO, and CO_2. The evolution vs. time of the hydrogen formation rate is shown in Fig. 4 for all compounds. LBTCss is the most active in H_2 production. An increase of its activity with time is to be noticed, which indicates a progressive modification of the surface upon exposure to the reaction mixture until reaching a stable state after 3 h. By contrast, the LBTCM sample exhibits a fairly constant rate of H_2 formation with time on stream, indicating neither activation nor deactivation. The activity of this sample is lower than LBTCss after 3 h of reaction. A slight activation is observed for LBTMss during the first 30 min, but this is followed by a slight deactivation before H_2 formation rate stabilizes at a level lower than for LBTCM. The non-substituted LBTss compound is by far the less active of the series. It can be concluded that the substitution by Ce and/or Mn in LBT strongly promotes the catalytic activity in H_2 production from CH_4/H_2O mixture, thus leading to more active materials in CH_4/H_2O reactions.

The thermodynamically favored reactions at 900 °C in a $CH_4/H_2O/N_2$ mixture are as follows:

$$CH_4 + H_2O \rightarrow CO + 3H_2 \quad (2)$$

$$CH_4 + 2H_2O \rightarrow CO_2 + 4H_2 \quad (3)$$

$$CH_4 \rightarrow C + 2H_2 \quad (4)$$

Several side reactions can also proceed but they are omitted for clarity [42]. In the experimental conditions used in the present work (50% CH_4/5% H_2O), the formation of carbon deposits is thermodynamically favored [75]. Nevertheless, in the present work, the quite stable activity of the solids once the steady state is reached suggests the absence of formation of carbon deposits during the reaction. In order to address this point, the most active catalyst of the series (LBTCss) was chosen for study by O_2-TPO experiment after preliminary treatment in N_2 and catalytic test of the sample at 900 °C for 180 min ($CH_4:H_2O = 10:1$). It revealed no O_2 consumption up to 900 °C, indicating that no significant carbon deposit had been formed during catalytic test (see Fig. S1 in supplementary information). The same result was previously reported for gadolinia-doped ceria GDC [75]. The absence (or very low) formation of such deposits indicates that the conversion of the $CH_4/H_2O/N_2$ mixture is mainly controlled by kinetics and not by thermodynamics.

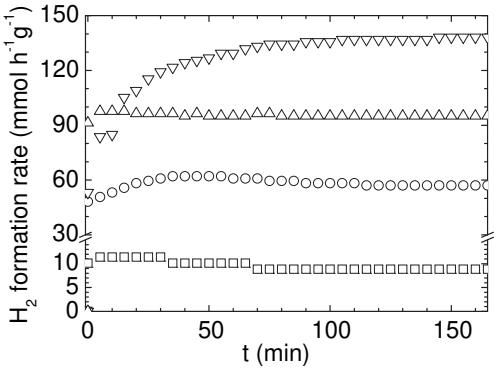

Fig. 4. Hydrogen formation rate as a function of time upon reaction of a 50:5:45 $CH_4:H_2O:N_2$ mixture over LBTss (□), LBTCss (▽), LBTMss (○), and LBTCM (△) samples. $T = 900$ °C, 20 mg sample, total flow rate = 6.2 L h^{-1}.

The experimental results on LBT-type materials, especially when doped with Mn and/or Ce, are considered to reflect their catalytic properties, which are found highly resistant to carbon formation similarly to GDC.

H_2, CO, and CO_2 formation rates, measured after 180 min reaction for LBTss, LBTCss, LBTMss, and LBTCM samples, are given in Table 2 and compared with $Ce_{0.9}Gd_{0.1}O_{1.95}$ (GDC) as reference sample [76]. For perovskite samples, the CO_2 formation rate varies weakly (from 11 up to 18 mmol h^{-1} g^{-1}) while the CO formation rates is strongly dependent on the sample. As a result, the CO/CO_2 molar ratio varies from 0.3 (for LBTMss) up to 2.3 (for LBTCss). It can be inferred that substitution by Ce strongly favors the production of CO. Comparison with the co-substituted sample suggests that Mn would inhibit the formation of CO or favor that of CO_2, confirming the Mn ability to oxidize CO [77–80]. Once more, as attested by CO/CO_2 ratio, doubly substituted LBTCM behavior is found intermediate between LBTCss and LBTMss. It is worth noting that, for LBTss, only H_2 could be detected; the too small amounts of CO and CO_2 could not be quantified.

Since O_2-TPO indicated the absence of C formation during these experiments, CO and CO_2 are the only C-containing products arising from CH_4 conversion. Rates of CH_4 disappearance ($-dn_{CH4}/dt$) after stabilization in the reaction mixture can be thus calculated according to the formula:

$$-dn_{CH4}/dt = dn_{CO}/dt + dn_{CO2}/dt \quad (5)$$

with dn_{CO}/dt and dn_{CO2}/dt equal to the rates of CO and CO_2 formation, respectively.

Values are reported in Table 2. The rate of CH_4 consumption obtained with the LBTss sample cannot be calculated but estimated from H_2 production. Values ranging between 2 and 3 mmol h^{-1} g^{-1} are obtained by assuming the likely hypothesis that only steam reforming (Eq. (2)) or reverse methanation (Eq. (3)) reactions proceed. Significant variation of the catalytic rate of CH_4 consumption can be observed depending on the material. This cannot be related to the surface area, which only slightly varies between samples (from 9.9 to 15.7 m^2 g^{-1}). No relationship can be found either between the catalytic performance of the materials and their respective TG behavior, described in Section 3.2. Nevertheless, whatever the tested compound, the catalytic activity in CH_4/H_2O reactions is markedly enhanced by substitution. LBTCss displayed the highest catalytic activity more than 1.5 and 13–20 times higher than GDC and LBTss, respectively. Although less studied than Mn substitution [81,82], the Ce doping appears especially efficient in improving the catalytic performance in methane steam reforming, more than Mn doping. Concerning the doubly substituted LBTCM compound, it displays intermediate performance between LBTCss and LBTMss, which seems to highlight prejudicial effect of either Ce-Mn association or stoichiometry of the titanate.

Table 2
Specific surface area of tested catalysts and rates of H_2, CO and CO_2 formation and CH_4 consumption.

Material	Specific surface area (m^2 g^{-1})	Formation rate[a] (mmol h^{-1} g^{-1})			CH_4 consumption rate[a] (mmol h^{-1} g^{-1})
		H_2	CO	CO_2	
LBTss	15.7	9	–[b]	–[b]	2–3[c]
LBTMss	9.9	57	4	11	15
LBTCss	11.8	139	27	13	40
LBTCM	12.5	95	8	18	26
GDC[d]	10.0	82	18	8	26

[a] The measurements were carried out at 900 °C after 180 min reaction using a CH_4:H_2O:N_2 = 10:1:9 gas mixture, 20 mg catalyst, dry flow rate = 6.2 L/h.
[b] Below detection limits.
[c] Estimated from H_2 formation rate assuming steam reforming or reverse methanation reactions.
[d] Pure gadolinia-doped ceria (GDC) is used for comparison. The surface area was measured after treatment at 900 °C in N_2.

3.4. Electrical behavior

Fig. 5 shows the evolution of total conductivity for LBTCss, LBTMss, and LBTM, measured in Ar/H_2(98/2) and air as a function of temperature. Whatever the atmosphere, LBTCss displays the highest conductivity values ($\sigma = 1.94.10^{-1}$ S cm^{-1} and $9.9.10^{-3}$ S cm^{-1} at 840 °C, in Ar/H_2(98/2) and air, respectively). LBTM ($\sigma = 2.2.10^{-2}$ S cm^{-1} and $6.9.10^{-4}$ S cm^{-1} at 780 °C in Ar/H_2(98/2) and 800 °C in air, respectively) and LBTMss ($\sigma = 4.2.10^{-3}$ S cm^{-1} and $3.9.10^{-4}$ S cm^{-1} at 825 °C in Ar/H_2(98/2) and 800 °C in air, respectively) are much less conductor.

Activation energy (E_a) values of 1.02, 0.90, and 0.78 eV were found in air for LBTM, LBTMss, and LBTCss, respectively. In Ar/H_2(98/2), it increases to E_a = 1.20 and 1.26 eV for LBTM and LBTMss, respectively. In contrast, for LBTCss, the activation energy measured in the same reducing atmosphere showed completely different values, varying with temperature from E_a ~0.8 eV above 780 °C to ~0.2 eV below, what is possibly due to a structural change around this temperature (not studied).

The electrical conductivity of LBTss was not studied in the frame of this work. Nonetheless, numerous results in literature concern this compound. Electrical behavior of $La_{0.05}Ba_{0.95}Ti_{0.9875}O_3$ strongly depends on the preparation route. Conductivity values at ~600 °C in air can vary from ~10^{-7} to ~3.10^{-3} S cm^{-1} when a liquid route synthesis is used followed by heat treatment at 1100 °C for 2 h in air [79] vs. solid-state synthesis followed by sintering at 1350 °C for 3 days in flowing O_2, respectively [83]. In the first case, the bad performances were related to residual inhomogeneities remaining after synthesis due to insufficient thermal treatment. In the present study, sol–gel synthesis combined with high temperature sintering treatment avoids the presence of such inhomogeneities. As a consequence, the comparison was carried with the latter results of LBTss prepared by solid-state synthesis.

Electrical conductivity values displayed by LBTMss and LBTM at 600 °C in air remain two order of magnitude inferior to the unsubstituted compound value from $La_{0.05}Ba_{0.95}Ti_{0.9875}O_3$ (at ~600 °C σ_{LBTMss} ~ $3.9.10^{-5}$ S cm^{-1} and σ_{LBTM} ~ 6.10^{-5} S cm^{-1} vs. σ_{LBTss} ~ 3.10^{-3} S cm^{-1} [83]. Similarly to $BaTi_{1-x}Mn_xO_3$ ($0 \le x \le 0.01$), the lower performance of the Mn-substituted materials could be related to the negative influence of the localized Mn electronic level between valence band and conduction band. Potentially reducible in air (in contrast to Ti) and in low quantity (5 at%), Mn atoms could act as deep electron trapping centers [84]. This phenomenon did not occur when Ti was substituted by Ce, Ce^{3+} levels remaining probably closer to the conduction band, without strong effect on electronic transfer within the titanate. Consequently, E_a in air were similar for both compounds (E_a(LBTCss) = 0.78 eV and $E_a(LBTss)_{0< x \le 0.20}$ ~ 0.7 eV [73]) and σ only slightly differed (σ_{LBTCss} ~ $1.0.10^{-3}$ S cm^{-1} at 600 °C in air, extrapolated value).

Electrical conductivity measurements performed in Ar/H_2(98/2) favored the performance of LBTCss vs. LBTMss and LBTM with $1.94.10^{-1}$ S cm^{-1} at 840 °C. Although this value remains low compared to the state-of-the-art anode materials, it stays above the minimum-value of 10^{-2} S cm^{-1} suggested by Gross et al. [22,85] in their experimented cell configuration. Whereas LBTM stayed up to this conductivity limit, LBTMss remained below. Although carrier concentration $[Ce^{3+}]_{LBTCss}$ = 1.3% was inferior to $[Mn^{3+}]_{LBTMss}$ = 2.7% and $[Mn^{3+}]_{LBTM}$ = 4.4%, LBTCss displayed better performances. These observations showed the superiority of $4f^1$-Ce^{3+} electronic level, possibly closer to conduction band than Mn electronic level.

3.5. Electrochemical properties

As mentioned just before, an electrical conductivity deficiency is not prejudicial with the cell configuration adopted. Then despite low electrical conductivity, the compounds were tested in symmetrical electrochemical cells in wet hydrogen conditions, characteristic of an

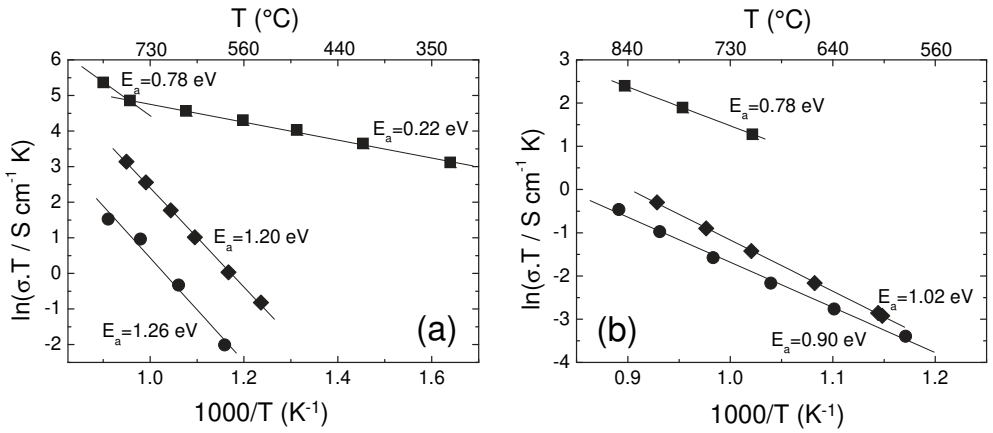

Fig. 5. Arrhenius plot of electrical conductivity for (♦) LBTM, (●) LBTMss, and (■) LBTCss measured (a) in Ar/H_2(98/2) and (b) in air. Activation energy values (E_a) were determined from the Arrhenius law.

SOFC anode. As indicated by preliminary tests, lanthanum barium titanate materials react chemically with YSZ electrolyte. Thus, a barrier layer of $BaIn_{0.3}Ti_{0.7}O_{3-\delta}$ (BIT) was first deposited on each face of YSZ discs, before being sintered at 1350 °C for 3 h in air, to avoid any reactivity between the electrolyte and the tested materials. In this case, a reactivity between YSZ and BIT is not excluded but would probably incorporate Zr (and possibly Y) into the barium titano-indate, i.e., would form a $Ba(In,Ti,Zr)O_{3-\delta}$ solid solution that has been recently studied and shows reasonably high ionic conductivity level similar to YSZ itself [86]. Each circular electrode (10 mm in diameter) was then deposited on the barrier layer, and then sintered at 1250 °C for 3 h in air with a temperature ramp of 300 °C h^{-1}, as indicated from preliminary shrinkage measurements. Secondary electrons SEM image of the fractured symmetrical cell corresponding to LBTCss material is given in Fig. 6 that is characteristic of all prepared cells. The image attests for the good contact and good adhesion between the YSZ electrolyte and the $BaIn_{0.3}Ti_{0.7}O_{3-\delta}$ (BIT) barrier layer (2 μm thick) as well as between the barrier layer and the tested electrode materials. The probed material electrode layers were about 7 μm thick and a homogeneous porous electrode microstructure was achieved in each case.

Complex impedance spectra were collected from 900 °C to 600 °C in H_2/H_2O(97/3) for LBTss, LBTCss, LBTMss, and LBTCM. For clarity, Fig. 7 displays the spectra obtained at 900 °C for LBTss and LBTCss, which exhibit the best performance. The electrochemical behavior was similar for the Mn-doped compounds. The EIS results were analyzed using the Z-view software based on complex non-linear least-squares fitting with an equivalent circuit made of a series resistance, R_s, connected with R_iQ_i parallel circuits, R_i being a resistor and Q_i a constant phase element of rate-limiting step i (Fig. 8(a)). A good fit was obtained with only two contributions, which constitute the polarization resistance R_p, one at high frequencies (HF) ($\Delta f_{HF} = 10^2$–10^4 Hz) followed by a greater medium-low frequencies (MLF) contribution ($\Delta f_{MLF} = 10^{-2}$–10^1 Hz). The evolution with temperature of the main characteristic electrochemical parameters for LBT/BIT/YSZ/BIT/LBT symmetrical cells is depicted in Fig. 8(b–d), LBT being LBTss, LBTCss, LBTMss, or LBTCM. The equivalent circuit parameters deduced from EIS spectra simulation at 900 °C are reported in Table 3 for all compounds. The quite high values of R_s are explained in part by the low electrical conductivity of the electrode materials, which is higher for the Mn-doped compound and by contact resistance at the different interfaces (e.g., at 900 °C, R_s value should be around 0.5 Ω cm^2 considering the only electrolyte contribution). Considering the existence of the MLF limiting process, the electrochemical behavior of pure or doped LBT seems slightly different from what has been described for pure or doped cubic-like LSTs, with generally two contributions observed at high and medium ($f_c > 1$ Hz) frequencies,

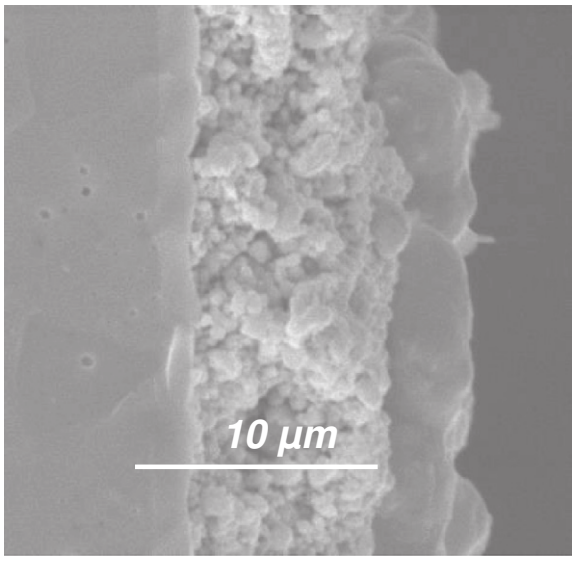

Fig. 6. SEM image of fractured LBTCss/BIT/YSZ/BIT/LBTCss symmetrical cell observed in secondary electrons mode.

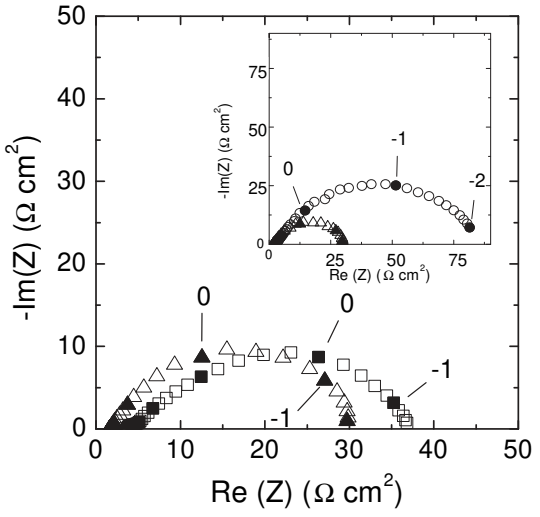

Fig. 7. Complex impedance spectra for LBTss (△) and LBTCss (□) collected on symmetrical cells (including YSZ electrolyte, BIT barrier layer and material electrodes) at 900 °C in H_2/H_2O(97/3). In inset: impedance spectra of LBTss at 900 °C in H_2/H_2O(97/3) (△) and $Ar/H_2/H_2O$(95/2/3) (○). Closed symbols and numbers indicate selected values of frequency ($\log_{10}$ scale).

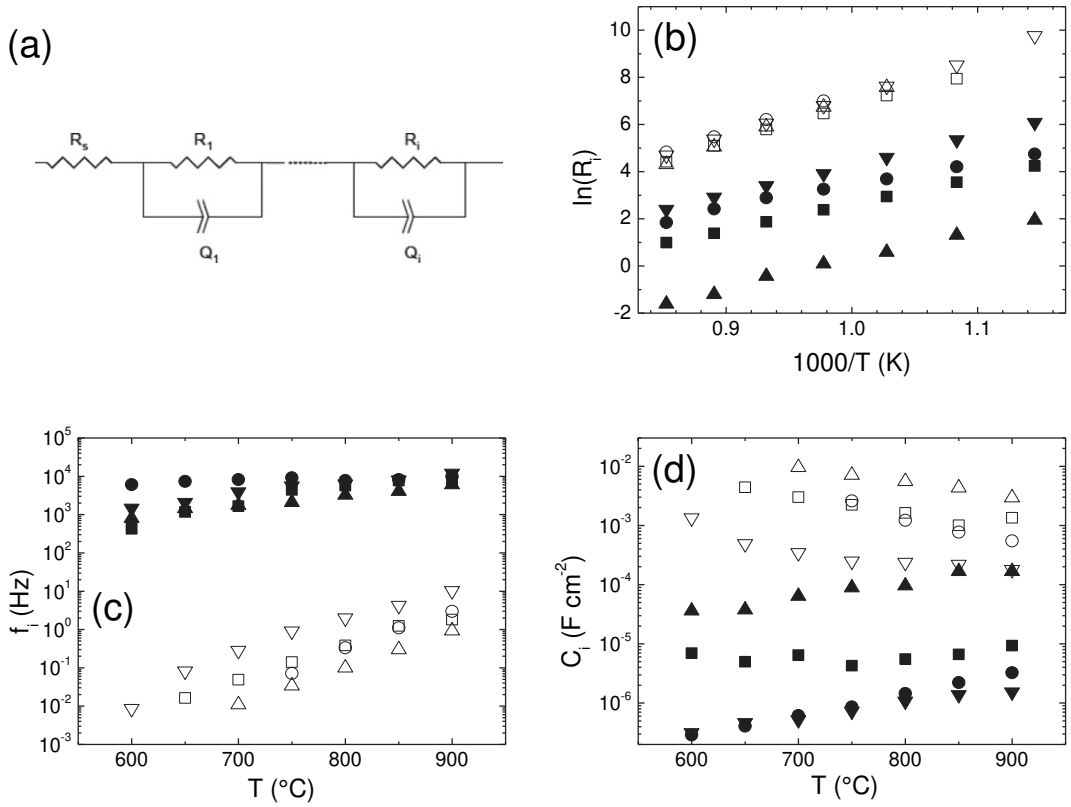

Fig. 8. Evolution with temperature of main characteristic electrochemical parameters for LBTss/BIT/YSZ/BIT/LBTss (△,▲), LBTCss/BIT/YSZ/BIT/LBTCss (□,■), LBTMss/BIT/YSZ/BIT/LBTMss (○,●), and LBTCM/BIT/YSZ/BIT/LBTCM (▽,▼) symmetrical cells studied in $H_2/H_2O(97/3)$. (b) Specific resistances R_i (Arrhenius plot), (c) apex frequencies f_i, and (d) specific capacitances C_i. Closed and open symbols are for HF and LF contributions, respectively. In (a), the equivalent circuit scheme applied to fit impedance spectra ($i = 2$ in our case).

that correspond to charge transfer and surface diffusion of hydrogen, respectively [38,49]. Nevertheless, for highly Mn-doped cubic-type LSTs, Fu et al. [87] described an additional low-frequency contribution ($f_c < 1$ Hz) similar to our case, which they associated to gas conversion impedance.

Considering their high-frequency range (~10^3–10^4 Hz), as well as the specific capacity and activation energy values, around 1.10^{-5} F cm^{-2} and 1 eV, respectively, R_{HF} linear evolution can be indubitably associated to a double layer capacity (charge transfer), most probably at the titanate/BIT interface, as for $Sr_{0.94}Ti_{0.9}Nb_{0.1}O_3$ [36] or lamellar LST [49]. Whereas literature generally report beneficial effects of Mn or Ce doping on electrochemical behavior [27,38,49,87,88], this is not the case here in LBTs series, the lower R_{HF} value being attributed to non-doped LBTss. On the other hand, B-site sub-stoichiometry in the perovskite seems to enhance the charge transfer process, taking in such conclusions all the necessary precautions, in view of the general difficulty of direct comparison between tested materials, even using the same cell preparation and testing conditions.

Considering now the MLF contribution, the characteristic frequency range (~10^{-2}–10 Hz) is relatively similar to the limiting component observed at low frequency for LSTM materials [87] and then could be related to the same gas conversion process. Nevertheless, in our case, neither the calculated activation energy values, ranging from 1.32 to 1.62 eV, nor the capacitance values, around 10^{-4}–10^{-2} F cm^{-2}, are in agreement with a gas conversion limiting step (for LSTM, capacitances around 1.5–2.5 F cm^{-2} and negative activation energy values were calculated [87]). The capacitance value does not correspond either with a thermally activated "chemical capacitance" generally observed in mixed conductors, as described by Jamnik and Maier [89,90]. On the other hand, LBTs values agree more with a strongly activated process such as the dissociative adsorption of hydrogen on the electrode surface [87], or surface diffusion of hydrogen from the adsorption point to the triple phase boundary, such as for lanthanum strontium titanates [49]. Such attribution would explain the influence of pH_2 observed on the MLF contribution when comparing the EIS data of LBTss for wet diluted or pure H_2 (see inset of Fig. 7).

In terms of performance, non-doped LBTss exhibits the lowest R_p values within the studied series (28.6 Ω cm^2 at 900 °C). Although not exceptional, it is markedly better than reported values for pure cubic perovskite-like La/Sr titanates [19,91], and similar to the value for lamellar LST [49]. The effect of Ba doping on the anodic performance of an $La_{0.4}Sr_{0.6}TiO_3$ perovskite has been recently described by Vincent et al. [45] in different case of fuels and according to their work no real benefit has been obtained in dry H_2. On the other hand, the same authors observed an interesting improvement of the anodic behavior using H_2S containing fuels (H_2 or CH_4), that could be similar to our own results for wet (3% H_2O containing) H_2 when comparing barium to strontium titanates. We tentatively interpret those results as an enhancement of the anode properties of the material related to the highest basicity of Ba-containing LBTs with respect to LSTs; such electrocatalytic improvement using a basic phase has been recently described in the case of Ba-doped Ni/YSZ cermet [92].

Table 3
Equivalent circuit parameters deduced from EIS spectra simulation for all symmetrical cells measured in $H_2/H_2O(97/3)$ at 900 °C. Resistances are given in Ω cm^2, capacitances in F cm^{-2}, and activation energies E_a for R_s, R_{HF}, and R_{LF} in eV.

Compound	R_s	E_a	HF			LF			R_p
			R_{HF}	C_{HF}	E_a	R_{LF}	C_{LF}	E_a	
LBTss	3.2	0.42	0.1	2.10^{-4}	0.97	28.5	3.10^{-3}	1.6	28.6
LBTCss	7.4	0.63	1.1	9.10^{-6}	0.96	33	1.10^{-3}	1.3	34.1
LBTCM	11	0.92	4.3	2.10^{-6}	1.1	43	2.10^{-4}	1.4	47.3
LBTMss	15	0.84	2.4	3.10^{-6}	0.82	49	5.10^{-4}	1.5	51.4

4. Conclusions

The pure and Mn and/or Ce-doped cubic-like perovskites $La_{0.05}Ba_{0.95}Ti_{1-x}M_yO_3$ were studied for possible use as SOFC anode materials. After synthesis in air, using a Pechini route, the structure of all compounds is found perfectly cubic with space group *Pm-3m*. Such high symmetry is retained in diluted hydrogen at 900 °C with almost no change in volume for the undoped or Ce-doped compound but a systematic small increase of cell volume ($\Delta V/V = 0.10$–0.24%) for all the Mn-doped titanates, associated to the Mn^{4+} to Mn^{3+} reduction, that is judged acceptable for the application.

Electrical and electrochemical performances of lanthanum barium titanates were strongly affected by the substitution. In particular, Mn substitution led to poor electronic mobility compared to unsubstituted perovskite which could be explained by local defects due to the presence of the substituting elements which could perturb the electron mobility. Interestingly, catalytic performance was highly promoted when cerium was introduced in the structure: as an example, catalytic activity in methane steam reforming conditions was more than 20 times higher when 5 at% of Ce was substituted for Ti in LBTss. When tested in symmetrical electrochemical cells under wet hydrogen conditions, cerium-doped compounds exhibit similar values for polarization resistance as the undoped compound. Because of their rather good catalytic properties, Ce-doped lanthanum barium titanates present interest as SOFC anode operating with methane. A further step would be to optimize the Ce content in the series, and also to try to apply the benefit of Ba for Sr and Ce for Ti substitutions to the case of lamellar LSTs, materials of potential interest upon the classical three-dimensional cubic-like LSTs [49,91].

Supplementary data to this article can be found online at http://dx.doi.org/10.1016/j.ssi.2015.11.005.

Acknowledgments

The authors are grateful to J. Toyir and K. Girona for their contribution to catalytic measurements, M. Dalmasso and T. Delahaye for their help in cell elaboration and electrochemical measurements. BIT powder has been kindly provided by the Institut des Matériaux Jean Rouxel, Nantes. C.P.-M. is grateful to ADEME and CEA for the PhD grant. The «Fonds Européen de Développement Régional (FEDER)», «CNRS», «Région Nord Pas-de-Calais», and «Ministère de l'Education Nationale de l'Enseignement Supérieur et de la Recherche» are acknowledged for funding of X-ray diffractometers.

References

[1] B.C.H. Steele, Solid State Ionics 86–88 (1996) 1223–1234.
[2] G. Pudmich, B.A. Boukamp, M. González-Cuenca, W. Jungen, W. Zipprich, F. Tietz, Solid State Ionics 135 (2000) 433–438.
[3] J.F. Rasmussen, A. Hagen, J. Power Sources 191 (2009) 534–541.
[4] R. Mukundan, E.L. Brosha, F.H. Garzon, Electrochem. Solid-State Lett. 7 (2004) A5–A7.
[5] J. Canales-Vázquez, S.W. Tao, J.T.S. Irvine, Solid State Ionics 159 (2003) 159–165.
[6] O.A. Marina, N.L. Canfield, J.W. Stevenson, Solid State Ionics 149 (2002) 21–28.
[7] S. Hashimoto, L. Kindermann, F.W. Poulsen, M. Mogensen, J. Alloys Compd. 397 (2005) 245–249.
[8] S. Hui, A. Petric, J. Electrochem. Soc. 149 (1) (2002) J1–J10.
[9] Q.X. Fu, S.B. Mi, E. Wessel, F. Tietz, J. Eur. Ceram. Soc. 28 (2008) 811–820.
[10] Q. Ma, F. Tietz, D. Stöver, Solid State Ionics 192 (2011) 535–539.
[11] Q. Ma, F. Tietz, Solid State Ionics 225 (2012) 108–112.
[12] X. Zhou, N. Yan, K.T. Chuang, J. Luo, RSC Adv. 4 (2014) 118–131.
[13] S. Roudeau, J.C. Grenier, J.M. Bassat, J. Fuel Cell Sci. Technol. 11 (2014) 041006.
[14] Q. Ma, B. Iwanschitz, E. Dahjav, S. Baumann, D. Sebold, I.A. Raj, A. Mai, F. Tietz, J. Power Sources 279 (2015) 678–685.
[15] M.C. Verbraeken, T. Ramos, K. Agersted, Q. Ma, C.D. Savaniu, B.R. Sudireddy, J.T.S. Irvine, P. Holtappels, F. Tietz, RSC Adv. 5 (2015) 1168–1180.
[16] J. Canales-Vázquez, M.J. Smith, J.T.S. Irvine, W. Zhou, Adv. Funct. Mater. 15 (2005) 1000–1008.
[17] J.C. Ruiz-Morales, J. Canales-Vázquez, C. Savaniu, D. Marrero-López, W. Zhou, J.T.S. Irvine, Nature 439 (2006) 568–571.
[18] C. Périllat-Merceroz, P. Roussel, M. Huvé, E. Capoen, Rose-Noëlle Vannier, G. Gauthier, Solid State Ionics 247–248 (2013) 76–85.
[19] O.A. Marina, L.R. Pederson, in: J. Huijsmans (Ed.), Proceedings of the 5th European Solid Oxide Fuel Cell Forum, Lucerne, Switzerland 2002, p. 481.
[20] J. Liu, B.D. Madsen, A. Ji, S.A. Barnett, Electrochem. Solid-State Lett. 5 (2002) A122–A124.
[21] B.D. Madsen, S.A. Barnett, J. Electrochem. Soc. 154 (2007) B501–B507.
[22] M.D. Gross, J.M. Vohs, R.J. Gorte, J. Mater. Chem. 17 (2007) 3071–3077 (and references therein).
[23] Q. Fu, F. Tietz, D. Sebold, S. Tao, J.T.S. Irvine, J. Power Sources 171 (2007) 663–669.
[24] P. Holtappels, J.T.S. Irvine, B. Iwanschitz, L. Theil Kuhn, L. Lu, Q. Ma, ECS Trans. 57 (1) (2013) 1175–1184.
[25] L. Lu, M.C. Verbraeken, M. Cassidy, J.T.S. Irvine, ECS Trans. 57 (1) (2013) 1415–1422.
[26] J.T.S. Irvine, P.R. Slater, A. Kaiser, J.L. Bradley, P. Holtappels, M. Mogensen, in: A.J. McEvoy (Ed.), Proceedings of the 4th European Solid Oxide Fuel Cell Forum, Oberrohrdorf, Switzerland 2000, p. 471.
[27] A. Ovalle, J.C. Ruiz Morales, J. Canales Vázquez, D. Marrero-Lopez, J.T.S. Irvine, Solid State Ionics 177 (2006) 1997–2003.
[28] M.J. Escudero, J.T.S. Irvine, L. Daza, J. Power Sources 192 (2009) 43–50.
[29] T.W. Pike, P.R. Slater, Int. J. Low Carbon Technol. 7 (2012) 60–62.
[30] S. Hui, A. Petric, Solid State Ionics 143 (2001) 275–283.
[31] F. Yi, H. Chen, H. Li, J. Fuel Cell Sci. Technol. 11 (2014) 031006.
[32] R.H. Mitchell, A.R. Chakhmouradian, J. Solid State Chem. 144 (1999) 81–85.
[33] V.V. Kharton, A.V. Kovalevsky, A.P. Viskup, F.M. Figueiredo, J.R. Frade, A.A. Yaremchenko, E.N. Naumovich, Solid State Ionics 128 (1–4) (2000) 117–130.
[34] C.Y. Park, D.X. Huang, A.J. Jacobson, L. Hu, C.A. Mims, Solid State Ionics 177 (2006) 2227–2233.
[35] P. Blennow, K.K. Hansen, L.R. Wallenberg, M. Mogensen, Solid State Ionics 179 (2008) 2047–2058.
[36] P. Blennow, A. Hagen, K.K. Hansen, L.R. Wallenberg, Solid State Ionics 180 (2009) 63–70.
[37] X. Li, H. Zhao, N. Xu, X. Zhou, C. Zhang, N. Chen, Int. J. Hydrog. Energy 34 (2009) 6407–6414.
[38] D.N. Miller, J.T.S. Irvine, J. Power Sources 196 (2011) 7323–7327.
[39] A. Yaqub, N.K. Janjua, C. Savaniu, J.T.S. Irvine, Int. J. Hydrog. Energy 40 (2015) 760–766.
[40] M.C. Verbraeken, T. Ramos, K. Agersted, Q. Ma, C. Savaniu, B. Reddy Sudireddy, RSC Adv. 5 (2014) 1168–1180.
[41] O.A. Marina, J.W. Stevenson, in: E.D. Wachsman, et al., (Eds.), Electrochemical Society Proceedings, Vol. 26, Pennington, NJ, USA 2002, p. 91.
[42] C. Périllat-Merceroz, G. Gauthier, P. Roussel, M. Huvé, P. Gélin, R.N. Vannier, Chem. Mater. 23 (2011) 1539–1550.
[43] R.D. Shannon, Acta Crystallogr. A 32 (1976) 751–776.
[44] S. Koutcheiko, Y. Yoo, A. Petric, I. Davidson, Ceram. Int. 32 (2006) 67–72.
[45] A. Vincent, J.-L. Luo, K.T. Chuang, A.R. Sanger, J. Power Sources 195 (2010) 769–774.
[46] J.-H. Li, X.-Z. Fu, J.-L. Luo, K.T. Chuang, A.R. Sanger, J. Power Sources 213 (2012) 69–77.
[47] M.K. Rath, B.-G. Ahn, B.-H. Choi, M.-J. Ji, K.-T. Lee, Ceram. Int. 39 (2013) 6343–6353.
[48] C. Mao, X. Dong, T. Zeng, Mater. Lett. 61 (2007) 1633–1636.
[49] C. Périllat-Merceroz, P. Roussel, M. Huvé, E. Capoen, S. Rosini, P. Gélin, R.N. Vannier, G.H. Gauthier, J. Power Sources 274 (2015) 806–815.
[50] J. Rodriguez-Carjaval, Physica B 192 (1993) 55–69;
J. Rodriguez-Carjaval, Newsletter 26 (2001) 12–19.
[51] M. Zahid, I. Arul Raj, F. Tietz, P. Lersch, D. Stöver, in: S.C. Singhal, J. Mizusaki (Eds.), Proc. of the 9th Int. Symp. on Solid Oxide Fuel Cells (SOFC-IX), vol. 2, The Electrochemical Society, Pennington, USA 2005, pp. 1708–1716.
[52] B.C. Tofield, W.R. Scott, J. Solid State Chem. 10 (1974) 183–194.
[53] J.E. Sunstrom, S.M. Kauzlarich, Chem. Mater. 5 (1993) 1539–1544.
[54] G.H. Jonker, E.E. Havinga, Mater. Res. Bull. 17 (1982) 345–350.
[55] C.R.A. Catlow, G.W. Lewis, J. Phys. Chem. Solids 47 (1986) 89–97.
[56] D. Markovec, Z. Samardzija, U. Delalut, D. Kolar, J. Am. Ceram. Soc. 78 (1995) 2193–2197.
[57] G.H. Jonker, Solid State Electron. 7 (1964) 895–903.
[58] O. Saburi, J. Phys. Soc. Jpn. 14 (1959) 1159–1174.
[59] V.J. Tennery, R.L. Cook, J. Am. Ceram. Soc. 44 (1961) 187–193.
[60] J. Daniels, K.H. Hardtl, D. Hennings, R. Wernicke, Philips Res. Rep. 31 (1976) 487–559.
[61] M.M. Nasrallah, H.U. Anderson, A.K. Agarwal, B.F. Flandermeyer, J. Mater. Sci. 19 (1984) 3159–3165.
[62] D. Markovec, Z. Samardzija, D. Kolar, J. Solid State Chem. 123 (1996) 30–38.
[63] D.F.K. Hennings, B. Schreinemacher, H. Schreinemacher, J. Eur. Ceram. Soc. 13 (1994) 81–88.
[64] Y. Jin, Y. Zhu, X. Yang, C. Li, J. Zhou, J. Solid State Chem. 180 (2007) 301–306.
[65] S. Sreekantan, A. Fauzi Mohd Noor, Z. Arifin Ahmad, R. Othman, A. West, J. Mater. Process. Technol. 195 (2008) 171–177.
[66] J.H. Hwang, Y. Ho Han, J. Am. Ceram. Soc. 84 (2001) 1750–1754.
[67] D.-Y. Lu, X.-Y. Sun, M. Toda, J. Phys. Chem. Solids 68 (2007) 650–664.
[68] O. Parkash, D. Kumar, R.K. Dwidedi, K.K. Srivastava, P. Singh, S. Singh, J. Mater. Sci. 42 (2007) 5490–5496.
[69] M. Benamira, L. Thommy, F. Moser, O. Joubert, M.T. Caldes, Solid State Ionics 265 (2014) 38–45.
[70] S.B. Desu, D.A. Payne, J. Am. Ceram. Soc. 73 (1990) 3407.
[71] N. Kuruta, M. Kuwabara, J. Am. Ceram. Soc. 76 (1993) 1605.
[72] F.D. Morrison, D.C. Sinclair, J.M.S. Skakle, A.R. West, J. Am. Ceram. Soc. 81 (1998) 1957–1960.
[73] F.D. Morrison, D.C. Sinclair, A.R. West, J. Appl. Phys. 86 (1999) 6355–6366.

[74] A.J.H. Mante, J. Volger, Phys. Lett. A24 (1967) 139–140.
[75] K. Girona, J. Laurencin, J. Fouletier, F. Lefebvre-Joud, J. Power Sources 210 (2012) 381–391.
[76] B. Mosqueda, J. Toyir, A. Kaddouri, P. Gélin, Appl. Catal. B Environ. 88 (2009) 361–367.
[77] B.W. Krupay, R.A. Ross, Can. J. Chem. 51 (1973) 3520–3527.
[78] D. Mehandjiev, I. Spassova, R. Kvatchkov, React. Kinet. Catal. Lett. 44 (1991) 337–343.
[79] N.D. Ivanova, S.V. Ivanov, E.I. Boldyrev, G.V. Sokol'skii, I.S. Makeeva, Russ. J. Appl. Chem. 75 (2002) 1420–1423.
[80] M. Wojciechowska, W. Przystajko, M. Zielinsky, Catal. Today 119 (2007) 338–341.
[81] J.R. Mawdsley, T.R. Krause, Appl. Catal. A Gen. 334 (2008) 311–320.
[82] J. Sfeir, P.A. Buffat, P. Möckli, N. Xanthopoulos, R. Vasquez, H.J. Mathieu, J. Van Herle, K. Ravindranathan Thampi, J. Catal. 202 (2001) 229–244.
[83] H. Beltran, E. Condorcillo, P. Escribano, D.C. Sinclair, A.R. West, J. Am. Ceram. Soc. 87 (2004) 2132–2134.
[84] X. Wang, M. Gu, B. Yang, S. Zhu, W. Cao, Microelectron. Eng. 66 (2003) 855–859.
[85] M.D. Gross, J.M. Vohs, R.J. Gorte, J. Electrochem. Soc. 154 (2007) B694–B699.
[86] A. Jarry, E. Quarez, O. Joubert, Solid State Ionics 256 (2014) 76–82.
[87] Q.X. Fu, F. Tietz, D. Stöver, J. Electrochem. Soc. 153 (2006) D74–D83.
[88] E. Lay, M. Benamira, C. Pirovano, G. Gauthier, L. Dessemond, Fuel Cells 12 (2) (2011) 265–274.
[89] J. Jamnik, J. Maier, J. Electrochem. Soc. 146 (1999) 4183–4188.
[90] J. Jamnik, J. Maier, Phys. Chem. Chem. Phys. 3 (2001) 1668–1678.
[91] C. Périllat-Merceroz, P. Roussel, R.N. Vannier, P. Gelin, S. Rosini, G. Gauthier, Adv. Energy Mater. 1 (2011) 573–576.
[92] M.V. Sandoval, A. Matta, T. Matencio, R. Zacarias Domingues, G.A. Ludwig, M. de Angelis Korb, C. de Fraga Malfatti, P. Gauthier-Maradei, G.H. Gauthier, Solid State Ionics 261 (2014) 36–44 (and references therein).